aerospace

MDPI

Article

An Adaptive Multi-Objective Reconstruction Evolutionary Method for Integrating Dense Remote Sensing Satellites into Low-Earth Orbit Mobile Communication Constellations

Aowei Shen [1], Jiao Wang [2], Yuan Tian [1], Gan Yu [1], Xiaowei Shao [3] and Dexin Zhang [1,*]

[1] School of Automation and Intelligent Sensing, Shanghai Jiao Tong University, Shanghai 200240, China
[2] China Satellite Network Innovation Co., Ltd., Beijing 100029, China
[3] School of Aeronautics and Astronautics, Shanghai Jiao Tong University, Shanghai 200240, China
* Correspondence: dx_zhang@sjtu.edu.cn

Abstract

Using low-Earth orbit (LEO) mobile communication constellations to transmit remote sensing satellite data represents an emerging paradigm for overcoming the bottleneck in downloading massive amounts of Earth observation data. However, dense concurrent access across multiple satellites triggers intense resource competition, severe visible-window fragmentation, and strict resource-exclusivity constraints. To address the complex scheduling challenges caused by high laser link establishment overhead and the high-dynamic motion between remote sensing satellites and LEO communication nodes, this paper proposes an Adaptive Multi-Objective Reconstruction Evolutionary Algorithm (AMOREA). The algorithm incorporates a hybrid initialization strategy to improve the quality of the initial solution set and designs a mission-level topology reconstruction mechanism that uses four complementary decomposition operators and a multi-strategy reconstruction pool to achieve effective resource aggregation. Furthermore, an adaptive weight feedback mechanism is introduced to dynamically adjust search priorities and balance global exploration with local exploitation. Simulation results show that, under the simulation settings of this study, AMOREA reaches a 100.0% completion rate for urgent high-priority tasks and an overall average task completion rate of 89.2%. In terms of multi-objective optimization performance, AMOREA obtains the highest mean hypervolume (HV) value among the compared algorithms, improving the mean HV by approximately 19.1% over NSGA-II, 17.6% over MOEA/D, and 67.6% over the Greedy baseline. These results indicate that AMOREA can generate higher-quality Pareto solution sets and improve the efficiency of high-dynamic inter-satellite transmission scheduling under the tested simulation settings.

Keywords: remote sensing satellites; satellite data downlink; low-Earth orbit (LEO) mobile communication constellations; laser inter-satellite links; multi-objective optimization

Academic Editor: Stefano Silvestrini

Received: 28 May 2026
Revised: 26 June 2026
Accepted: 30 June 2026
Published: 3 July 2026

1. Introduction

With the rapid advancement of Earth observation technology [1], a new generation of remote sensing satellites has achieved significant breakthroughs in spatial, temporal, and spectral resolution, leading to a surge in the average daily data volume per satellite [2]. However, in the face of rapidly expanding transmission demands, existing data transmission systems are increasingly revealing performance bottlenecks. Traditional satellite-to-ground communication models rely heavily on the geographical distribution

of ground stations, resulting in scarce and fleeting line-of-sight windows [3]; while geostationary orbit (GEO) relay systems can achieve wide-area coverage, their long-distance transmission is accompanied by significant link loss and latency [4]. In recent years, the large-scale deployment of LEO communication constellations, represented by Starlink [5] and OneWeb [6], has provided a highly promising new space-based access path for the efficient downlink of remote sensing data [7], leveraging the low propagation loss, low communication latency, and global coverage characteristics inherent to LEO [8].

Regarding satellite data transmission scheduling, existing research has primarily focused on two major scenarios, direct satellite-to-ground transmission [9] and satellite-to-GEO relay [10], and a relatively mature algorithmic framework has been established. In the case of direct satellite-to-ground transmission, although mixed-integer programming [11,12] and two-phase decomposition [13] can find optimal solutions, they are computationally inefficient and are thus mostly used for benchmark comparisons on small- to medium-scale problems. For large-scale scheduling, heuristic [14,15] and meta-heuristic [16] algorithms have become mainstream. For example, Xiang et al. [17] proposed a task-oriented data compression framework that reduces the amount of downlink data by selecting features from regions of interest, while Zhang et al. [18] employed an improved genetic algorithm to address integrated scheduling problems.

As data transmission requirements evolve from single-downlink events to continuous support, research has shifted toward the efficient integration of data transmission resources. Sun et al. [10] addressed the resource scarcity problem at ground access nodes through a multi-objective evolutionary algorithm, specifically for scenarios integrating ground station telemetry and data transmission resources; Chen et al. [19] proposed a data-oriented scheduling algorithm that emphasizes the integrity and timeliness constraints of data transmission access, ensuring that massive amounts of observational data can be transmitted back in an orderly manner through limited access windows; Chen et al. [20] further investigated dynamic rescheduling methods under mission-adaptive conditions, generating Pareto solutions that prioritize different objectives. Additionally, Zhou et al. [21] proposed an algorithm to integrate fragmented idle resources, thereby alleviating ground station pressure by improving resource utilization. Although these studies have improved the system's scheduling capabilities by optimizing the logic for allocating communication resources, their research scenarios have primarily focused on satellite-to-ground links.

In recent years, to enhance the real-time performance and intelligence [22] of solutions, intelligent optimization methods such as feature extraction based on support vector machines [23], machine learning operators [24], and deep reinforcement learning [25,26] have been gradually introduced, improving the ability to search the solution space under complex constraints. Research on satellite-GEO relay scheduling focuses on utilizing the wide-area coverage characteristics of GEO satellites to alleviate data backlogs [27], with the core challenge lying in resource congestion management at GEO nodes; for homogeneous inter-satellite links, existing work is mostly limited to cooperative routing within satellite clusters or single constellations [28], where nodes typically employ cooperative protocols and exhibit relatively simple motion patterns. However, research on scheduling in cross-tier, heterogeneous networks integrating remote sensing satellites into LEO mobile communication constellations [29] remains in its infancy. Unlike GEO relays or links within homogeneous constellations, remote sensing satellites and LEO mobile communication constellations form a heterogeneous network with high dynamics at both ends [30].

Therefore, integrating remote sensing satellites into LEO mobile communication constellations poses significant technical challenges. Unlike wide-beam microwave links, remote sensing satellites typically employ narrow-beam laser inter-satellite links [31]. This characteristic necessitates a complex pointing, acquisition, and tracking (PAT) process [32]

to establish the link, thereby introducing a non-negligible time overhead. In the highly dynamic LEO-LEO environment, network topologies change rapidly. Although frequent switching to the communication node with the shortest current geometric distance helps achieve higher instantaneous data rates, frequent link switching introduces cumulative link-establishment time losses and may even increase the risk of communication interruptions. Therefore, finding the optimal balance between instantaneous rate gains and the costs of link switching is key to improving the system's transmission efficiency.

Furthermore, this challenge is exacerbated in concurrent multi-satellite scenarios. As the scale of remote sensing constellations expands, the dense spatial distribution of satellites leads to severe temporal overlap in their access requests to the same LEO communication nodes. Coupled with the strict one-to-one physical exclusivity of laser communication terminals, multiple remote sensing missions frequently collide over limited access opportunities. This intense resource competition forces the system to constantly preempt and switch links among different satellites, aggressively fragmenting the available visible time windows. When this multi-satellite competition couples with the incompressible PAT overhead, standard scheduling strategies often fail to prevent massive capacity degradation.

To address these challenges, this paper proposes AMOREA, which integrates dense remote sensing satellites into LEO mobile communication constellations. This method resolves the conflict between laser link establishment overhead and time-domain window fragmentation decision-making in high-dynamic, two-end motion scenarios, and establishes a multi-objective optimization model that jointly balances priority-weighted transmission utility, slicing cost, and communication-node load imbalance. By introducing an adaptive reconstruction operator and a priority-based hierarchical mechanism, AMOREA can dynamically adjust search priorities in real time based on the characteristics of topological evolution, thereby achieving an optimal trade-off between system throughput gains and handover costs under physical hard constraints.

The remaining sections of this paper are organized as follows: Section 2 presents the problem statement and the construction of the scheduling model; Section 3 provides a detailed description of the AMOREA-based fine-grained scheduling framework, including its overall architecture and core innovative mechanisms; Section 4 evaluates the effectiveness of the proposed method through simulation experiments; and Section 5 concludes the paper.

2. Problem Description and Unified Modeling

2.1. Problem Description

This study focuses on the resource scheduling problem for remote sensing satellites accessing LEO mobile communication constellations to downlink data in highly dynamic environments. From a physical perspective, remote sensing satellites S and LEO communication nodes N are deployed at different altitudes and inclinations within LEO, resulting in high-speed motion at both ends, as shown in Figure 1. Under this high-speed, asynchronous motion of both ends, the relative spatial geometry between the satellite and the node undergoes drastic transient changes, resulting in highly time-varying, discrete, and finite Visible Time Windows (VTWs). The duration $t_{dur}^{j} = t_{j}^{end} - t_{j}^{start}$ of the set $W = w_1, w_2, \ldots, w_M$ of candidate windows varies, ranging from tens to hundreds of seconds, thereby defining the boundaries of the solution space for resource scheduling in the temporal domain.

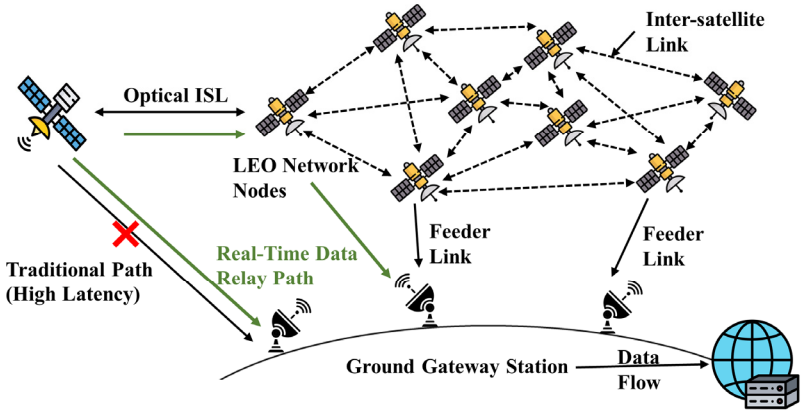

Figure 1. Remote sensing satellites integrated into LEO mobile communication constellations. The red cross indicates the traditional direct satellite-to-ground path with high latency caused by limited ground-station visibility. The green arrows represent the proposed real-time data relay path, where remote sensing data are forwarded through LEO network nodes and then transmitted to ground gateway stations. The black dashed arrows denote inter-satellite links within the LEO constellation, while the feeder links deliver data from LEO nodes to ground stations.

Against the backdrop of an ever-expanding fleet of remote sensing satellites, the spatial proximity of multiple satellites in orbit makes dense access a key factor in resource conflicts. This density leads to a high degree of temporal overlap in access requests from multiple remote sensing satellites to the same communication node, as shown in Figure 2. Furthermore, the exclusive nature of communication payload resources further intensifies the fierce competition between missions in both temporal and spatial dimensions. Consequently, the nature of the scheduling problem has evolved from single-mission path planning to the time-slot matching of complex concurrent access missions. The core challenge lies in achieving optimal time-slot matching and scheduling for finite communication resources, given a sequence of concurrent access missions and multiple constraints, including heterogeneity, high dynamics, and resource exclusivity.

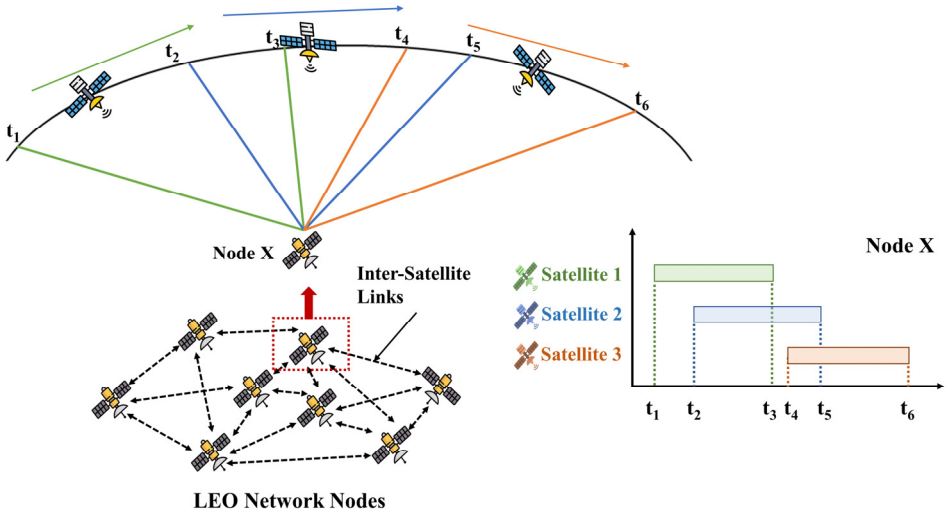

Figure 2. Conflict arising from multiple remote sensing satellites accessing the same node. The green, blue, and orange lines and arrows represent the visibility and access intervals of Satellites 1–3 to the same LEO node, respectively. The red dashed box highlights the selected example LEO node.

In actual transmission, narrow-beam laser communication systems are commonly used for inter-satellite links to support high-bandwidth data transmission. Unlike traditional radio frequency communication, laser links must undergo a rigorous PAT process. Each

link establishment incurs a fixed time overhead t_{PAT}, and a guard interval t_{guard} is typically required before and after link switching. In a dynamic topological environment caused by high-speed motion at both ends, this incompressible physical overhead further reduces the already fragmented visible windows, creating a core conflict between high-throughput downlink transmission and the overhead of frequent link switching. Constrained by both the evolutionary patterns of heterogeneous constellation topologies and the characteristics of laser communication systems, three key technical challenges are present.

The first challenge is the spatiotemporal clustering and resource-competition conflicts caused by heterogeneous orbital configurations. Due to the wide-area nature of remote sensing mission execution and the discrete distribution of communication nodes, access demands exhibit extreme spatial–temporal imbalance. In specific latitude bands or during peak mission periods, multiple remote sensing satellites converge on the same communication node within a short timeframe. This leads to explosive accumulation of system downlink traffic at specific spatiotemporal nodes, creating local hotspots, while other time periods or nodes remain idle. Local resource overload prevents some missions from obtaining transmission opportunities even when they possess geometric visibility. The primary challenge lies in maximizing system throughput while ensuring the fulfillment of high-priority missions.

Second is the challenge of resolving mutual-exclusion constraints arising from the physical exclusivity of laser inter-satellite links. Due to the limitation that a remote sensing satellite S_m is equipped with only a single inter-satellite link terminal, the system must satisfy strict resource exclusivity constraints: at any given moment, the satellite can establish an active link with only one node. Furthermore, communication nodes typically serve only a single satellite, meaning that at any given moment, a node can respond to the access request of only one remote sensing satellite. This creates a strong relationship of mutual exclusion and competition between the two sides over time. For a node n, all possible usage windows may exhibit arbitrary relationships on the timeline, forming a high-dimensional combinatorial space. Once usage rights for the node n during the time slot $\left[\tau_j^{start}, \tau_j^{end}\right]$ are allocated to the task i, this decision deprives other tasks visible to the node n during that time slot of access opportunities. In multi-satellite concurrent scenarios, multiple potential conflicts must be resolved with sub-second temporal precision; furthermore, once a high-priority task locks the transmission channel, other concurrent tasks must be delayed or redirected to other nodes.

Third is the issue of temporal fragmentation and performance degradation caused by dynamic switching. When a communication node is shared among multiple tasks, the complete visibility window of unselected tasks is fragmented by high-priority tasks, resulting in temporal fragmentation. Suppose the task i has a completely visible window $[t_0, t_1]$ for the node n, but because another task i' occupies the node during the time interval $[t_a, t_b] \subset [t_0, t_1]$, the task i''s original window is split into two segments: $[t_0, t_a]$ and $[t_b, t_1]$. Since the independent use of each fragment requires the full overhead of establishing and terminating a link, the effective capacity of a fragment is $C_{pot} = max\left(0, T_{frag} - t_{PAT} - t_{guard}\right) \cdot v$. Further, considering the minimum effective data slice threshold D_{min}, the corresponding minimum effective transmission duration is $t_{min}^j = D_{min}/v_j$. When the fragment loses its transmission value, it forms a dead zone. Therefore, the key to increasing the system's net capacity lies in suppressing the fragmentation of time slots through temporal reorganization—while meeting the concurrent requirements of multiple satellites—and aggregating discrete residual resources into effective transmission time slots.

2.2. Variable Definition and Mathematical Modelling

In data transmission scenarios, there is a massive demand for data transfer between LEO mobile communication constellations and remote sensing satellites. Based on potential future data transmission requirements, we have modeled and formally described the problem of scheduling data transmission resources for nodes in LEO mobile communication constellations. Each access task $r_i \in R$ is characterized by its data demand D, priority p, and assigned satellite $s(r)$. The essence of scheduling is to allocate available time and data-transmission capacity to each access task across these candidate windows while satisfying constraints such as resource exclusivity and link overhead.

To better establish the model, the variable definitions shown in Table 1 are first provided.

Table 1. Key symbols and meanings.

Variable Symbol	Variable Definition
S/s_m	Remote sensing satellite set/mth satellite
N/n_n	LEO communication node set/nth node
W/w_j	Visible Time Window set/jth window
R/r_i	Access task set/ith task
p_i	Priority of Task i
D_i	Data Volume of Task i
D_{min}	Minimum effective slice data volume
t^j_{dur}	Initial visibility duration of the jth window
v_{link}	Traditional fixed rate
v^j_{link}	Data transmission rate of window j
t_{PAT}	Laser link PAT time
t_{guard}	Satellite handover guard time
K_i	Slice index set of task i
$w_{i,k}$	Selected window index for kth slice of task i
$\tau_{i,k}$	Occupation start time of slice $w_{i,k}$
$d_{i,k}$	Actual transmitted data volume of slice $w_{i,k}$
$\xi_{i,k}$	Occupation end time of slice $w_{i,k}$
t^i_{ddl}	Deadline of task i
C^j_{eff}	Net effective capacity of window j
$C_{pot}(j)$	Potential transmission capacity of window j
Q_j	Quality score of window j
f_1	Negative priority-weighted transmission utility
f_2	Scaled number of transmission slices
f_3	Normalized node load imbalance
U_{ref}	Scaling factor for f_1
K_{ref}	Scaling factor for f_2
L_n	Total data assigned to communication node n
$\overline{L}$	Average load over all used or available nodes
S^j_T	Time-window duration score of window j
S^j_R	Range-quality score of window j
S^j_V	Radial velocity stability score
C_{max}	Maximum transmissible data capacity of a generated task block
P_i	Penalty for uncompleted urgent task
ρ_L	Standard deviation of communication-node load

To characterize the multi-segment data transmission process of remote sensing satellites within visible time windows, this paper uses a slicing approach to describe the scheduling results for each mission. Let the set of missions be $R = \left\{r_1, \ldots, r_{|R|}\right\}$. For any mission r_i, the set of available candidate visible time windows is denoted as $W_i \subseteq W$. Since window segmentation and resource competition often require a single task to be completed

in segments across multiple windows, this paper introduces a variable-size slice index set K_i for each task r_i, where the number of slices $m_i = |K_i|$ is determined adaptively by the optimization process. For any slice $k \in K_i$, this paper defines its decision variable as a triplet:

$$(w_{i,k},\ \tau_{i,k},\ d_{i,k})$$

Here, $w_{i,k} \in W_i$ denotes the visible time window number selected for the kth slice of task i, $\tau_{i,k}$ denotes the start time of the slice, and $d_{i,k} \geq 0$ denotes the actual amount of data transmitted for that slice. Due to variations in the communication environment during satellite overflights, traditional fixed-rate assumptions often do not align with actual physical scenarios. Therefore, this paper introduces a dynamic data transmission rate v_{link}^{j} based on the comprehensive quality score Q_j:

$$Q_j = \omega_T \cdot S_T^j + \omega_R \cdot S_R^j + \omega_V \cdot S_V^j \tag{1}$$

$$S_T^j = \frac{T_{dur}^j - T_{dur}^{min}}{T_{dur}^{max} - T_{dur}^{min}} \tag{2}$$

$$S_R^j = \frac{R_{max} - R_j}{R_{max} - R_{min}} \tag{3}$$

$$S_V^j = \frac{V_{max} - V_j}{V_{max} - V_{min}} \tag{4}$$

$$v_{link}^{j} = v_{link} \cdot \frac{log_2(1 + \eta_Q \cdot Q_j)}{log_2(1 + \eta_Q)} \tag{5}$$

Here, the weights of the three quality-score components are set as $\omega_T = 0.4$, $\omega_R = 0.3$, and $\omega_V = 0.3$, respectively, satisfying $\sum \omega = 1$. This setting assigns a slightly higher importance to the visible-window duration, because longer effective windows can provide more stable transmission opportunities after deducting the PAT overhead. The range-related score and radial velocity stability score are assigned equal weights to jointly characterize the link-quality and geometric-visibility conditions. The rate modulation coefficient η_Q is used to control the nonlinear sensitivity of the transmission rate to the comprehensive quality score Q_j.

The three quality components are normalized to the range [0, 1] before aggregation, so that the weighted score can consistently reflect the relative quality of different visible windows. The weights are not intended to represent hardware-calibrated physical constants; instead, they are used as simulation parameters to emphasize that longer effective windows are slightly more beneficial for reducing the influence of fixed PAT overhead, while range quality and radial-velocity stability jointly describe the instantaneous link condition. The rate modulation coefficient controls the nonlinear sensitivity of the transmission rate to the aggregated quality score, and its value is kept fixed for all compared algorithms to ensure a fair comparison.

The nonlinear modulation effect of link quality is simulated using a Shannon-like logarithmic formula; this formula is normalized to ensure the rate always remains within the valid range $[0,\ v_{link}]$. Given the rate v_{link}^{j} in a given window $w_{i,k}$ and a fixed link establishment overhead t_{PAT}, the end time of a slice's occupancy is determined by the physical link relationship as $\xi_{i,k} = \tau_{i,k} + t_{PAT} + \frac{d_{i,k}}{v_{link}^{j}}$. Based on the above definition, a candidate solution can be represented as the set of all task-slice variables:

$$x = \left\{ (w_{i,k},\ \tau_{i,k},\ d_{i,k}) \middle| r_i \in R,\ k \in K_i \right\} \tag{6}$$

2.2.1. Constraint Conditions

The modeling of the research problem involves multiple constraints, primarily including basic visibility constraints, link transmission duration constraints, resource concurrency and exclusivity constraints, and laser link establishment constraints. These resource constraints are formulated as scheduling constraints, as shown below.

(1) Window selection domain constraint: Each slice must be selected from the set of candidate windows for that task:

$$w_{i,k} \in W_i, \qquad \forall i \in R,\ k \in K_i \tag{7}$$

(2) The physical duration of the slice must fall entirely within the visible time range of the selected window:

$$t_{w_{i,k}}^{start} \le \tau_{i,k} < \xi_{i.k} \le t_{w_{i,k}}^{end}, \qquad \forall i \in R,\ k \in K_i \tag{8}$$

(3) Satellite exclusive protection constraint: A single remote sensing satellite may establish only one link at any given time, and must maintain a protection interval t_{guard} before and after switching to ensure stability and security.

$$[\tau_{i,k},\ \xi_{i,k}] \cap \left[\tau_{i',k'} - t_{guard},\ \xi_{i',k'} + t_{guard}\right] = \varnothing, \qquad \forall (i,k) \ne (i',k'),\ s(i) = s(i') \tag{9}$$

(4) Node-exclusive service constraint: At any given time, a single communication node may only respond to an access request from one satellite, ensuring mutual exclusion of resources on the node side.

$$[\tau_{i,k},\ \xi_{i,k}] \cap [\tau_{i',k'},\ \xi_{i',k'}] = \varnothing, \qquad \forall (i,k) \ne (i',k'),\ n(w_{i,k}) = n(w_{i',k'}) \tag{10}$$

(5) Constraint on non-overlapping slices within a task: Multiple slices of the same task must not overlap on the timeline, ensuring that the sequence of slices for a single task is consistent and executable.

$$[\tau_{i,k},\ \xi_{i,k}] \cap [\tau_{i,\ k'},\ \xi_{i,k'}] = \varnothing, \qquad \forall i \in R, k \ne k' \tag{11}$$

(6) Minimum effective slice constraint: The amount of data transmitted back for each slice must not be less than D_{min}, thereby preventing the waste of link establishment caused by a large number of inefficient fragments.

$$d_{i,k} \ge D_{min}, \qquad \forall i \in R,\ k \in K_i \tag{12}$$

(7) Upper limit constraint on task requirements: The cumulative amount of data transmitted back for a task must not exceed its requirement, thereby preventing unnecessary excess transmission.

$$\sum\nolimits_{k \in K_i} d_{i,k} \le D_i, \qquad \forall i \in R \tag{13}$$

(8) Data transmission deadline constraint: A task must complete its final segment or reach the specified completion rate before the deadline.

$$\max_{k \in K_i} \xi_{i,k} \le t_{ddl}^{i}, \qquad \forall i \in R \tag{14}$$

2.2.2. Optimization Objectives

To achieve efficient data backhaul under limited visible-window resources and strong mutual-exclusion constraints, this paper constructs a three-objective optimization model

from the perspectives of task transmission benefit, link establishment cost, and node load balance.

Firstly, given that different tasks have varying business value to the system, task $i \in R$ is assigned a priority weight of p_i, and its set of allocated slices is denoted as K_i. On this basis, f_1 is defined as the maximization of the total priority-weighted backhaul volume:

$$U(x) = \sum_{i \in R} (\sum_{k \in K_i} p_i d_{i,k} - P_i) \tag{15}$$

Here, $d_{i,k}$ denotes the actual amount of data transmitted by the kth slice of task i, and D_i denotes the total data demand of task i. The first term in $U(x)$ accumulates the priority-weighted backhaul volume of all scheduled slices, thereby encouraging the algorithm to allocate more transmission resources to high-value tasks.

$$P_i = \begin{cases} M \cdot p_i \cdot \left(1 - \frac{\sum_{k \in K_i} d_{i,k}}{D_i}\right), & p_i \geq 8, \ \frac{\sum_{k \in K_i} d_{i,k}}{D_i} < 0.99 \\ 0, & else \end{cases} \tag{16}$$

P_i represents the conditional penalty charged exclusively for unfinished urgent tasks, and M is the penalty factor. Specifically, the penalty is imposed only when task i is an urgent task, i.e., $p_i \geq 8$, and its completion ratio is lower than 99%. For all routine tasks with $p_i < 8$, or for urgent tasks that reach the required completion ratio, the penalty is identically zero.

$$min f_1(x) = -\frac{U(x)}{U_{ref}} \tag{17}$$

U_{ref} is used as a scaling factor for the first objective and is set to the maximum single-task priority-weighted backhaul volume observed in the current evaluated population. Since the evolutionary algorithm is formulated as a minimization problem, maximizing the backhaul utility is equivalently transformed into minimizing $-U(x)/U_{ref}$. Therefore, f_1 guides the algorithm to improve the total weighted transmission benefit while strengthening the protection of urgent and high-priority tasks.

Secondly, although slicing-based scheduling enhances feasibility and flexibility in fragmented visible windows, it also introduces additional overhead for link establishment and handover. Each slice corresponds to an independent link-occupancy process and incurs the corresponding physical overhead, such as PAT and switching protection. Therefore, the second objective is designed to minimize the scaled number of transmission slices:

$$min f_2(x) = \frac{\sum_{i \in R} |K_i|}{K_{ref}} \tag{18}$$

Here, $|K_i|$ denotes the number of slices allocated to task i. K_{ref} is used as a scaling factor for the second objective and is set to the maximum number of slices assigned to a single task in the current evaluated population. A larger value of f_2 indicates that the solution uses more fragmented transmission segments and may introduce more frequent link establishment and switching overhead. Therefore, minimizing f_2 encourages the algorithm to aggregate available resources into fewer effective transmission slices.

Thirdly, while slicing-based scheduling enhances feasibility and flexibility, it also introduces additional overhead for link establishment and handover, and may result in the spatial and temporal concentration of node load. To characterize this cost, the cardinality $|K_i|$ of set K_i represents the number of slices for that task. To mitigate localized concentration

of resource utilization at the node level, the load of a communication node $n \in N$ is defined as the sum of the data volumes of all slices that have selected that node:

$$L_n = \sum_{i \in R} \sum_{\substack{k \in K_i \\ n(w_{i,k}) = n}} d_{i,k}, \qquad \forall n \in N \tag{19}$$

Here, $n(j)$ denotes the communication node number corresponding to window j. Taking the average node load $\overline{L}$ as a reference:

$$\overline{L} = \frac{1}{|N|} \sum_{n \in N} L_n \tag{20}$$

Characterizing load imbalance using the overall standard deviation:

$$\rho_L = \sqrt{\frac{1}{|N|} \sum_{n \in N} \left(L_n - \overline{L}\right)^2} \tag{21}$$

Consequently, the third objective is defined as the normalized node load imbalance:

$$min f_3(x) = \frac{\rho_L}{\overline{L}} \tag{22}$$

Minimizing f_3 encourages the algorithm to distribute transmission loads more evenly across available communication nodes.

In summary, the proposed three-objective model jointly considers transmission benefit, link establishment cost, and node load balance. f_1 focuses on improving the priority-weighted task backhaul utility, especially for urgent and high-priority tasks; f_2 suppresses excessive slicing and frequent link establishment caused by fragmented windows; and f_3 mitigates node-level load imbalance. These objectives are mutually conflicting in dense and highly dynamic scheduling scenarios. Therefore, AMOREA seeks Pareto-optimal solutions that balance task-transmission benefit, switching overhead, and load distribution subject to physical feasibility constraints.

3. Multi-Objective Evolutionary Algorithm Based on Adaptive Reconstruction Mechanism

Given the highly fragmented inter-satellite link topologies, the overhead associated with laser link establishment, and the multi-objective conflicts characteristic of high-speed, dual-end motion scenarios, the single crossover and mutation operators of traditional genetic algorithms struggle to effectively search for high-quality Pareto-optimal solutions while maintaining temporal continuity of links. To address this issue, this section presents AMOREA. Building upon the framework of multi-objective optimization algorithms [33], this method integrates hybrid initialization, topological reconstruction operators, and an adaptive weight feedback mechanism. By intelligently selecting decomposition and refilling strategies during the evolutionary process, it achieves efficient scheduling while satisfying physical exclusivity constraints.

3.1. Algorithm Framework

As shown in Figure 3, AMOREA consists of three main stages: population initialization, adaptive decomposition–reconstruction evolution, and Pareto-based environmental selection. This section provides an overview of the workflow, while the following subsections detail the corresponding mechanisms.

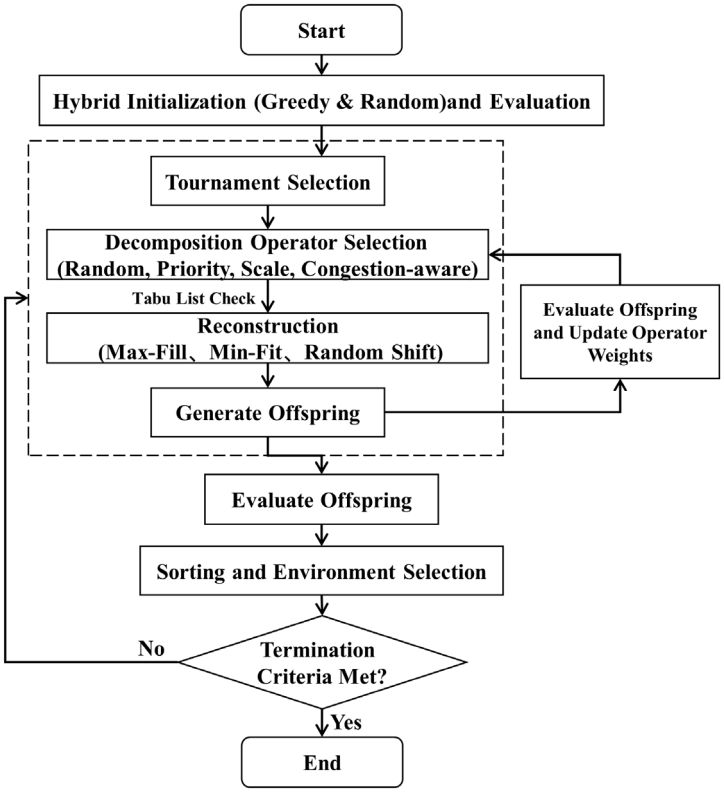

Figure 3. AMOREA flowchart.

To address the problem of resource scheduling for large-scale and complex inter-satellite links, AMOREA employs a multi-strategy operator pool to replace the fixed crossover and mutation operations of traditional genetic algorithms, thereby approximating the Pareto front of the problem through iterative search. The algorithm first performs hybrid initialization under spatiotemporal constraints, combining greedy construction and random exploration to generate an initial solution set that satisfies hard physical constraints.

The evaluation phase is based on a three-objective fitness vector that explicitly considers task transmission benefit, link establishment cost, and node load balance. Specifically, the first objective f_1 maximizes the priority-weighted backhaul utility while imposing a conditional penalty on unfinished urgent tasks; the second objective f_2 minimizes the reference-scaled total number of transmission slices to reduce link establishment and handover overhead caused by fragmented visible windows; and the third objective f_3 minimizes the normalized node load imbalance to encourage a more even distribution of transmission loads among communication nodes. Superior individuals are then identified through non-dominated sorting and Pareto-based environmental selection.

Upon entering the core evolutionary process, the algorithm dynamically selects decomposition operators based on an adaptive weight feedback mechanism, releasing spatiotemporal resources according to task granularity to form incomplete solutions. Subsequently, during the reconstruction phase, a multi-strategy competition mechanism is introduced. Through sequential trials of rules such as maximum filling, minimum fitting, and random offset, promising offspring solutions are generated. This process also incorporates online updates of operator weights. Through continuous iterative optimization, AMOREA ultimately seeks Pareto-optimal solutions that balance the three conflicting objectives of transmission benefit, link establishment cost, and node load distribution.

3.2. Core Mechanism of the Algorithm

3.2.1. Hybrid Initialization Mechanism

In LEO networks characterized by high-speed movement at both ends, the visible time window is significantly fragmented. If an initial solution is generated using a purely random approach, it is highly likely to produce invalid schedules with capacities below the minimum slice capacity D_{min}, leading to search stagnation in the early stages of the algorithm. Therefore, AMOREA employs a hybrid initialization strategy that combines deterministic greedy and random exploration to balance the quality and diversity of the initial solution set. Deterministic greed aims to identify link resources with high transmission potential. For access task r_i, the algorithm first calculates the potential transmission capacity $C_{pot}(j)$ for each window in the candidate window set W_i and sorts them in descending order. Let the start and end times of window$j$ be $\left[t_j^{start},\ t_j^{end}\right]$, and the link dynamic rate be v_{link}^j; then, the potential transmission capacity after deducting the hard link establishment overhead is:

$$C_{pot}(j) = v_{link}^j \times max\left\{0,\ \left(t_j^{end} - t_j^{start} - t_{PAT}\right)\right\} \tag{23}$$

During the actual insertion process, the algorithm maintains a global spatiotemporal occupancy table for nodes and satellites, and uses an idle slot calculation function to extract available contiguous idle sub-intervals within the window. A slice is only permitted to be generated if a given idle sub-interval $\left[t^{start}, t^{end}\right]$ still satisfies the minimum data transmission requirement after accounting for link establishment overhead; that is, it must satisfy the following physical constraint:

$$\left(t_j^{end} - t_j^{start} - t_{PAT}\right) \cdot v_{link}^j \geq D_{min} \tag{24}$$

This greedy path tends to prioritize filling windows with larger net effective capacity, ensuring that the initial population includes a subset of individuals with high-throughput characteristics. To prevent the greedy strategy from causing the population to become trapped in a local optimum prematurely and overlook sub-optimal yet critical connection opportunities, the algorithm introduces a randomization mechanism. This mechanism follows a uniform distribution in window selection, while still performing strict physical validity checks during the time-slot allocation phase. The algorithm randomly selects a starting point from the available free time slots within candidate windows, while rigorously verifying that the remaining capacity satisfies the constraints. Through this controlled randomness, the algorithm is able to generate physically feasible and diverse solutions within complex spatiotemporal gaps, providing a rich selection of genes for subsequent evolutionary processes.

3.2.2. Decomposition and Reconstruction Operator

As shown in Figure 4, address window fragmentation and multi-task competition conflicts caused by highly dynamic topological evolution, AMOREA has designed a topological operator mechanism that combines task-level decomposition with multi-strategy competitive reconstruction. Unlike slice-level fine-tuning, this method employs task-granular structural clearance: once an access task r_i is selected, all currently allocated slices for that task are removed in their entirety to completely release the spatiotemporal resources they occupy, thereby providing a larger search neighborhood for resolving complex resource deadlocks. The decomposition phase comprises four complementary decomposition operators designed to address different types of inefficient structures and conflict bottlenecks.

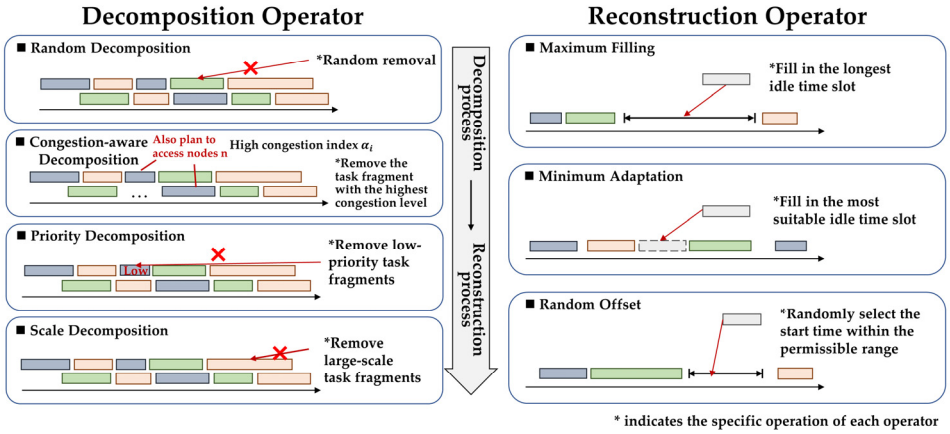

Figure 4. Decomposition and reconstruction strategy diagram.

One category focuses on global exploration, comprising stochastic decomposition and congestion-aware decomposition. Stochastic decomposition disrupts the current local steady state by introducing unbiased random perturbations, aiming to prevent the algorithm from getting stuck at local optima; congestion-aware decomposition, based on the inter-task conflict intensity metric α_i, specifically removes competing tasks at bottleneck nodes to resolve scheduling conflicts by reducing the intensity of local resource competition. The potential conflict intensity α_i of task i is defined as the statistical measure of time overlap between its candidate window and the candidate windows of other tasks at the same node. A binary variable $\delta_{j,j'}$ is introduced to represent the conflict state between windows.

$$\delta_{j,j'} = \begin{cases} 1, & n(j) = n(j'), \ \left[t_j^{start}, t_j^{end}\right] \cap \left[t_{j'}^{start}, t_{j'}^{end}\right] \neq \varnothing \\ 0, & else \end{cases} \tag{25}$$

Based on this, the congestion metric for task i is calculated as follows:

$$\alpha_i = \frac{p_i}{\alpha_{max}} \sum_{j \in W_i} \sum_{i \neq i'} \sum_{j' \neq W_{i'}} \delta_{j,j'} \tag{26}$$

Here, α_{max} represents the maximum conflict intensity. This operator prioritizes the removal of tasks with higher α_i values, aiming to reduce resource competition at critical nodes and alleviate scheduling deadlocks caused by multiple satellites competing for the same node.

Another category focuses on local optimization, comprising priority decomposition and scale decomposition. Priority decomposition follows a business-value-oriented approach, prioritizing the release of time slots occupied by low-priority tasks to reserve contiguous transmission space for critical tasks, thereby optimizing the weighted backhaul benefit f_1. Scale decomposition, on the other hand, re-schedules high-capacity tasks to guide the system toward more compact resource utilization, thereby improving the overall time slot fill rate.

To avoid ineffective oscillations between clearing and immediate refilling near local optima, a tabu list mechanism is introduced during the decomposition phase. Specifically, the maximum length of the tabu list is set according to a predefined tabu ratio, i.e., 15% of the total number of access tasks in this study. After a decomposition operator removes a set of scheduled tasks, the indices of these removed tasks are used to construct the tabu list. If the number of removed tasks exceeds the predefined maximum tabu list size, a random subset of the removed task indices is selected. During the subsequent reconstruction process of the current offspring, the tasks contained in the tabu list are excluded from the repair candidate set, thereby preventing them from being immediately reinserted into the same

solution. This mechanism forces the algorithm to explore alternative task combinations and resource occupation patterns. The tabu list is used only as a local short-term memory for the current offspring and is discarded after the reconstruction process is completed, preventing it from permanently restricting the global search space.

The reconstruction phase employs a multi-strategy competition mechanism to repair the incomplete solution x'. The algorithm concurrently evaluates rules such as Max-Fill, Min-Fit, and Random-Shift, and selects the optimal strategy based on the heuristic utility function ψ:

$$\psi(z) = \Delta D(z) - \lambda \cdot \Delta|K| \tag{27}$$

Here, z represents a candidate solution generated by a certain restructuring strategy; $\Delta D(z)$ denotes the additional amount of valid backhaul data generated by the system after adopting solution z; $\Delta|K|$ denotes the number of new slices introduced by solution z; and λ is the handover cost coefficient. By aggregating discrete residual resources during restructuring, this process extends the effective connection duration of a single link, thereby fundamentally mitigating the performance degradation caused by the overhead of establishing laser links.

3.2.3. Adaptive Weight Feedback Mechanism

Inter-satellite link scheduling is a non-stationary dynamic optimization process: in the early stages of evolution, the focus should be on global search to cover a broad feasible domain, while in the later stages, the emphasis should shift to local exploration to refine the approximation of the Pareto front. To adapt to these phased changes in requirements, AMOREA implements an adaptive weight feedback mechanism for the decomposition operator pool.

This mechanism maintains a dynamic weight $\omega_{m,g}$ for each decomposition operator op_m (where m is the decomposition operator index). At the end of each evolutionary generation, the system assigns tiered rewards based on the contribution of the offspring solutions to Pareto dominance over the current elite population. The specific evaluation criteria are as follows: if an offspring solution dominates all solutions in the elite population, it is assigned the highest score σ_1; if it dominates some solutions, it is assigned the second-highest score σ_2; if it is neither dominated nor dominating the elite solutions and enters the non-dominated frontier, it is assigned the intermediate score σ_3; if it is dominated by an elite solution, it is assigned σ_4. This yields the average reward $\pi_{m,g}$ for operator op_m in the gth generation, and the weights are updated using the exponential smoothing moving average formula:

$$\omega_{m,g+1} = (1 - \lambda_\omega) \cdot \omega_{m,g} + \lambda_\omega \cdot \pi_{m,g} \tag{28}$$

Here, $\lambda_\omega \in (0, 1)$ is the reaction factor, used to control the decay rate of historical information. After the update, the weights are normalized such that $\sum_m \omega_{m,g+1} = 1$, and the selection probability of the next-generation solution decomposition operator is determined via a roulette wheel mechanism. This closed-loop feedback mechanism endows the algorithm with online learning capabilities: during periods of severe congestion or when solution quality stagnates, random decomposition and congestion-aware decomposition often yield higher rewards, thereby increasing their selection probability to enhance exploration; conversely, as the solution set converges, priority-based and scale-based decompositions can more effectively improve the objective function value through fine-tuning, thereby dominating the search process. This mechanism ensures that the algorithm achieves a dynamic balance between exploration and exploitation within a limited computational budget.

3.3. Computational Complexity Analysis

Let P denote the population size, G denote the maximum number of generations, R denote the number of access tasks, W denote the average number of candidate visible windows per task, and K denote the average number of scheduled slices in an individual. Since the number of objectives is fixed in this paper, it is treated as a constant.

In AMOREA, the initialization stage constructs each individual by scanning tasks and their candidate visible windows, and its complexity can be approximated as $\mathcal{O}(PRW)$. During each generation, the adaptive decomposition–reconstruction process searches feasible windows for selected tasks and updates the corresponding node and satellite occupancy states. Its main computational cost is approximately $\mathcal{O}(PRW)$ under the average-case analysis. The fitness evaluation scans the scheduled slices of each individual, with complexity $\mathcal{O}(PK)$. The Pareto-based environmental selection relies on non-dominated sorting, whose complexity is $\mathcal{O}\left(P^2\right)$ when the number of objectives is fixed.

Therefore, excluding the hypervolume calculation used only for performance evaluation, the overall computational complexity of AMOREA can be approximated as:

$$\mathcal{O}\left(PRW + G\left(PRW + PK + P^2\right)\right)$$

This analysis shows that the computational cost of AMOREA mainly depends on the population size, the number of access tasks, the number of candidate visible windows, and the population-based non-dominated sorting process. In the simulation experiments, P and G are fixed, so the runtime mainly increases with the scale of task-window combinations and the density of resource conflicts.

From a scalability perspective, when P and G are fixed as algorithmic control parameters, the dominant scale-dependent term is mainly related to the task-window combination size, i.e., RW, together with the population-level environmental selection term P^2. Therefore, as the constellation and task scales increase, the main computational pressure is expected to arise from denser task-window matching and more frequent conflict checking, which motivates future work on large-scale scenario testing and parallel implementation.

4. Simulation Experiments and Results Analysis

In the previous chapters of this paper, we have provided a detailed exposition of the relevant theoretical foundations. In this section, we apply this method to a typical data transmission scheduling scenario involving the integration of remote sensing satellites into LEO mobile communication constellations, conduct simulation experiments, and analyze the results.

4.1. Experimental Parameter Configuration

To objectively evaluate the performance of the scheduling method proposed in this paper, the interface between STK 11 and MATLAB R2018a was first configured through the STK/Connect module, enabling MATLAB-based programming and control of the STK 11 simulation environment. As shown in Figure 5, a high-fidelity satellite network simulation scenario was established in STK 11. The access-window data predicted by STK were then exported and used to generate the experimental test cases.

In the STK 11 simulation scenario, a LEO communication constellation consisting of 600 communication nodes was constructed. Specifically, 30 circular LEO orbital planes were configured at an altitude of 500 km and an inclination of 60°, with 20 communication nodes uniformly distributed in each orbital plane. The LEO communication constellation is shown in blue in Figure 5.

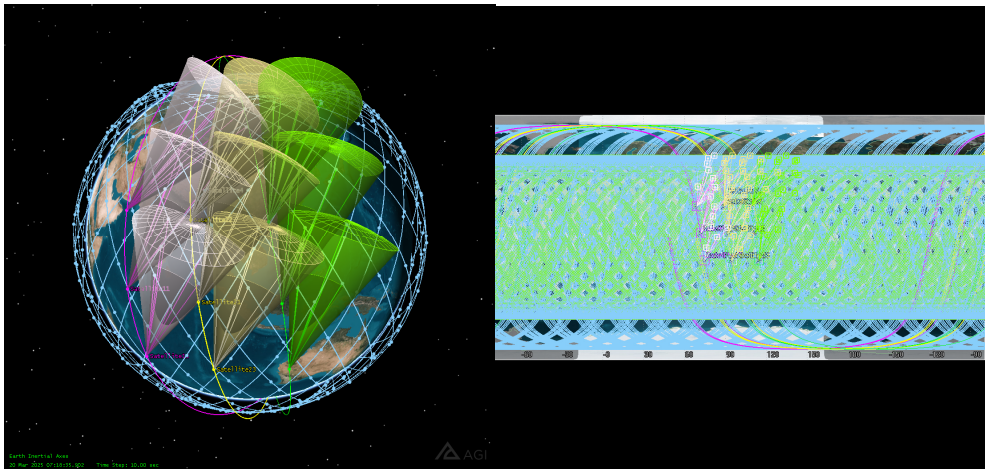

Figure 5. Satellite network simulation scenario built using STK 11. Pink, yellow and green correspond to Satellite 11, Satellite 12, Satellite 12, Satellite 21, Satellite 22, Satellite 23, Satellite 31, Satellite 32 and Satellite 33 from top to bottom respectively.

To validate the effectiveness of the proposed method, remote sensing satellites were configured in near sun-synchronous orbits with an altitude of 700 km and an inclination of 97.8°. The corresponding orbital and sensor parameters are listed in Table 2. In Figure 5, the remote sensing satellite groups and their corresponding sensor coverage cones are shown in pink, yellow, and green, respectively. The planning horizon for all scenarios was set to a 24-h interval from 04:00:00 on 20 March 2025 to 04:00:00 on 21 March 2025.

Table 2. STK 11 configuration parameters for remote sensing satellites and their sensors.

ID	RAAN	True Anomaly	Half-Angle	Azimuth	Elevation
Sensor 11	0°	0°	20°	30°	20°
Sensor 12	0°	20°	20°	30°	20°
Sensor 13	0°	340°	20°	30°	20°
Sensor 21	20°	0°	20°	30°	20°
Sensor 22	20°	20°	20°	30°	20°
Sensor 23	20°	340°	20°	30°	20°
Sensor 31	40°	0°	20°	30°	20°
Sensor 32	40°	20°	20°	30°	20°
Sensor 33	40°	340°	20°	30°	20°

To further demonstrate the complexity of the simulated scenario, we analyzed the full set of raw visible windows before scheduling optimization.

Figure 6a shows the visible-window length distribution of different remote sensing satellites. The results indicate that the available visible windows are highly fragmented: most windows are concentrated in relatively short-duration ranges, while only a limited number of long-duration windows are available. This fragmentation directly increases the difficulty of constructing continuous and efficient transmission schedules after deducting the PAT overhead.

Figure 6b further presents the spatial distribution of communication-node hotspots in the LEO communication constellation. In this heatmap, the horizontal axis represents the satellite index within each orbital plane, and the vertical axis represents the orbital-plane index. Therefore, each pixel corresponds to one LEO communication node. The color indicates the hotspot score of the corresponding node, with brighter colors indicating stronger potential resource competition.

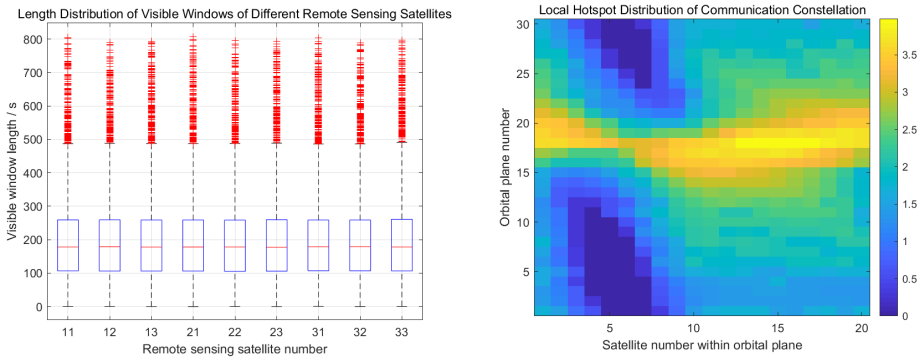

(**a**) (**b**)

Figure 6. Scenario-complexity analysis. (**a**) Visible-window length distribution of different remote sensing satellites. (**b**) Hotspot distribution of communication nodes based on visible-window overlap statistics.

The hotspot score is derived from visible-window overlap statistics. Specifically, for each communication node, we first identify all visible windows associated with different remote sensing satellites. If two visible windows from different remote sensing satellites overlap in time and correspond to the same communication node, they are counted as a competing window pair. Based on this definition, the hotspot score is calculated by jointly considering the number of overlapping visible-window pairs, the total overlap duration, the number of conflict windows, and the maximum number of remote sensing satellites concurrently visible at that node. Each component is normalized before aggregation.

As shown in Table 3 and Figure 6b, the resource competition is not uniformly distributed over the communication constellation. Several orbital-plane and satellite-index regions exhibit significantly higher hotspot scores, indicating that multiple remote sensing satellites tend to compete for the same communication nodes within overlapping time intervals. These local hotspots demonstrate the spatial concentration of access conflicts and further support the need for a scheduling method capable of balancing transmission benefit, link-establishment overhead, and node-level load distribution.

Table 3. Scenario-complexity statistics based on visible windows.

Indicator	Value
Total visible windows	34,211
Mean visible-window duration	202.48
Median visible-window duration	178.33
Ratio of windows shorter than 200 s	0.5680
Conflict-window ratio	0.8654
Number of participating visible communication nodes	573
Number of conflict communication nodes	555

In the experimental task sequence, test instances with different task scales were generated based on the STK-predicted access-window data. For each remote sensing satellite, high-quality candidate communication-node windows were selected, and task time blocks with a duration of at least 15 consecutive minutes were constructed. Urgent tasks were required to be transmitted within their corresponding time blocks, whereas routine tasks were allowed to be transmitted within one hour after the start time of the corresponding block. The maximum transmissible data capacity C_{max} of each time block was calculated as the product of the block duration and the average transmission rate of the covered access windows. The specific task-generation parameters are shown in Table 4.

Table 4. Specific parameter settings for different tasks.

Task Type	Priority p_i	Proportion	Generated Traffic Volume
Daily Tasks	1–5	0.8	(0.8–1.0) C_{max}
Urgent Tasks	8–10	0.2	0.6 C_{max}

Building on previous studies, this paper conducts a detailed performance evaluation and access-feasibility analysis for 600 LEO communication nodes. Considering the orbital evolution of remote sensing satellites during high-speed operation and the geometric constraints imposed by payload fields of view, a set of high-quality candidate communication nodes was identified for each remote sensing satellite. The results of this preprocessing stage provide a high-quality spatiotemporal resource pool for subsequent resource allocation, allowing the proposed algorithm to focus on time-slot mutual exclusion and conflict resolution in highly dynamic heterogeneous scheduling environments.

Unlike rapid reacquisition within an isomorphic constellation that only demands minor adjustments of the fine-pointing mechanism for the same target or adjacent nodes [34], this study addresses multi-satellite concurrent conflicts in highly dynamic heterogeneous networks. In this scenario, resolving scheduling conflicts typically requires the laser terminal to switch from one communication node to a new one. This cross-target switching necessitates large-angle mechanical rotation of the coarse-pointing mechanism [32], thereby requiring the introduction of a physical guard time t_{guard} [8], followed by a complete t_{PAT} for the new target.

Existing studies have shown that the establishment of laser inter-satellite links may involve setup delays on the order of tens of seconds, and a representative value of approximately 30 s has been reported for laser link establishment [8,34]. Therefore, $t_{PAT} = 30$ s is adopted in this study as a conservative per-link setup time for establishing a new cross-target laser link, rather than as the rapid reacquisition time for the same target. Because the previous PAT state cannot be directly reused after switching to a different communication node, the new link is modeled as requiring a complete PAT process. In addition, $t_{guard} = 20$ s is introduced as an engineering protection interval to account for coarse-pointing rotation, terminal settling, and safety margins before the next link establishment. These two parameters are used to model the non-negligible physical overhead caused by dynamic laser link establishment and switching in the simulated heterogeneous LEO-LEO scheduling scenario.

The key system parameters are shown in Table 5, and all experiments were simulated and validated using the MATLAB R2018a platform.

Table 5. Key system parameter settings.

Parameter	Symbol	Value
Downlink rate	r_{norm}	1 Gbps
Laser link establishment time	t_{PAT}	30 s
Laser switching protection time	t_{guard}	20 s
Rate modulation coefficient	η_Q	100
Population size	P	50
Maximum number of iterations	G_{max}	100
Switching cost factor	λ	10
Penalty factor	M	10,000

4.2. Analysis of Experimental Results

To comprehensively evaluate the convergence, diversity, and robustness of the obtained Pareto solution sets, this paper introduces the hypervolume (HV) metric. Since the

proposed scheduling model is formulated as a three-objective minimization problem, the HV is calculated in the three-dimensional objective space composed of f_1, f_2, and f_3, where f_1 denotes the negative priority-weighted transmission utility, f_2 denotes the transmission slicing cost, and f_3 denotes the node load imbalance. A larger HV value indicates that the obtained non-dominated solution set dominates a larger region with respect to the reference point and therefore reflects better overall Pareto quality.

For all algorithms, a unified global reference point is adopted to ensure fair comparison. According to the minimization form of the objectives and the task-size bounds, the reference point is set as $(0, |\mathcal{T}|, 1)$, where $|\mathcal{T}|$ is the number of access tasks. The first component corresponds to the no-transmission upper bound of the negative utility objective, while the second and third components provide conservative bounds for the slicing cost and load imbalance.

To reduce the influence of randomness in evolutionary optimization, each stochastic algorithm was independently executed 20 times with different random seeds under the same task scenario and parameter settings. The comparative algorithms include the proposed AMOREA, the slicing-enabled NSGA-II baseline, and the MOEA/D baseline. In addition, the deterministic Greedy algorithm was included as a heuristic baseline. Table 6 reports the mean and standard deviation of the final HV values for all compared algorithms, as well as the objective extrema obtained over the repeated trials.

Table 6. Statistical results of HV and objective extrema over 20 independent trials. The objective values reported in Table 6 are statistical indicators obtained over repeated trials and are used as auxiliary measures of the final Pareto-set quality. They do not necessarily correspond to the same individual solution selected by the composite-score criterion.

Algorithm	HV_mean	HV_std	f_1_mean	f_1_std	f_2_mean	f_2_std	f_3_mean	f_3_std
AMOREA	8484.6	152.94	−122.46	0.059846	26.221	0.56313	0.64387	0.0054857
NSGA-II	7126.6	153.62	−102.18	0.90943	105.65	1.0804	0.56024	0.0094864
MOEA/D	7217.4	330.27	−113.99	0.28543	61.875	1.9784	0.66203	0.016313
Greedy	5063.8	0	−102.33	0	268	0	0.53837	0

The results show that AMOREA achieves the highest mean HV value among all compared algorithms, reaching 8484.6 ± 152.94. In contrast, the mean HV values of NSGA-II, MOEA/D, and Greedy are 7126.6 ± 153.62, 7217.4 ± 330.27, and 5063.8 ± 0, respectively. Therefore, AMOREA improves the mean HV by approximately 19.1% over NSGA-II, 17.6% over MOEA/D, and 67.6% over Greedy. These results demonstrate that AMOREA obtains a better overall Pareto solution set in terms of convergence and diversity.

The HV standard deviation further reflects the robustness of the algorithms across independent trials. AMOREA exhibits a relatively small deviation compared with its mean HV value, indicating stable optimization performance under different random seeds. MOEA/D shows a larger HV deviation, suggesting that its decomposition-based search is more sensitive to stochastic initialization and evolutionary variation in this scheduling scenario. Greedy has zero deviation because it is deterministic under the same input scenario.

It should be noted that the reported f_1, f_2, and f_3 values are used as auxiliary indicators of the best objective extrema obtained by each algorithm over repeated trials. Since these extrema may correspond to different solutions within the Pareto set, they should not be interpreted as a single scheduling solution that simultaneously achieves all three objective values. Instead, the HV metric is used as the primary indicator for comparing the overall multi-objective optimization performance.

AMOREA obtains a set of non-dominated scheduling solutions rather than a single absolute optimum. Each solution on the Pareto front represents a different trade-off among

priority-weighted transmission benefit, slicing cost, and communication-node load balance. Therefore, the final scheduling plan reported in this paper is selected as a representative compromise solution from the non-dominated solution set.

To select this representative solution, a preference-based composite-score criterion is used as a post-processing decision rule. For each non-dominated solution x, its objective vector is denoted as $F(x) = (f_1(x),\ f_2(x),\ f_3(x))$, where the three objectives are expressed in minimization form. To avoid the influence of different numerical ranges, each objective is first normalized within the final non-dominated set using min–max normalization.

$$\overline{f}_m(x) = \frac{f_m(x) - f_m^{min}}{f_m^{max} - f_m^{min} + \varepsilon}, m = 1, 2, 3 \tag{29}$$

where f_m^{min} and f_m^{max} denote the minimum and maximum values of the mth objective among the final non-dominated solutions, respectively, and ε is a small positive constant used to avoid division by zero. The composite score of solution x is then calculated as:

$$S(x) = 0.50\overline{f}_1(x) + 0.25\overline{f}_2(x) + 0.25\overline{f}_3(x) \tag{30}$$

The larger weight assigned to the first objective reflects the primary preference for higher priority-weighted data return, because f_1 is formulated as the negative transmission utility in the minimization model, while the second and third objectives are used to penalize excessive slicing and communication-node load imbalance. Finally, the non-dominated solution with the smallest composite score is selected as the final representative scheduling solution:

$$x^{final} = \underset{x \in \mathcal{P}}{argmin} S(x) \tag{31}$$

where $\mathcal{P}$ denotes the final non-dominated solution set. This criterion is used only to select one representative scheduling plan for reporting and visualization, while the optimization process itself remains Pareto-based.

Figure 7 illustrates the solution-set distributions of AMOREA, NSGA-II, MOEA/D, and Greedy in the three-objective optimization space. AMOREA generates a more widely distributed and continuous Pareto front than the baseline algorithms. Compared with NSGA-II and MOEA/D, its solutions extend further toward the region with higher transmission benefit and fewer slices, indicating that the adaptive decomposition–reconstruction mechanism can more effectively aggregate fragmented visible windows and reduce unnecessary link establishment operations.

In contrast, the NSGA-II solutions are concentrated in a relatively limited region, reflecting weaker exploration capability in the expanded dense-access scenario. MOEA/D achieves a certain degree of Pareto distribution but provides fewer competitive solutions in the high-throughput and low-slicing region. Greedy produces only a single deterministic solution; although it may show relatively low load imbalance, it suffers from poorer transmission utility and a much larger slicing count. These results further illustrate the advantage of AMOREA in balancing transmission benefit, link-establishment cost, and node-load distribution.

Figure 8 presents a representative collaborative scheduling result generated by AMOREA in the multi-satellite access scenario. Figure 8a shows the task-level scheduling distribution over the 24-h planning horizon. The horizontal axis denotes time, and the vertical axis denotes the task index. Different colors correspond to different remote sensing satellites. The scheduled task slices are distributed throughout the entire planning period rather than being concentrated in a few short intervals, indicating that AMOREA can exploit temporally scattered visible windows under highly dynamic access conditions.

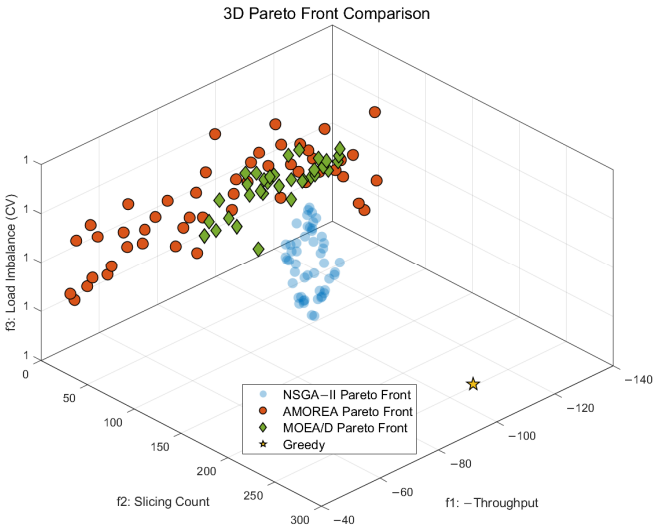

Figure 7. Comparison of the three-dimensional Pareto front distributions among AMOREA and the baseline algorithms.

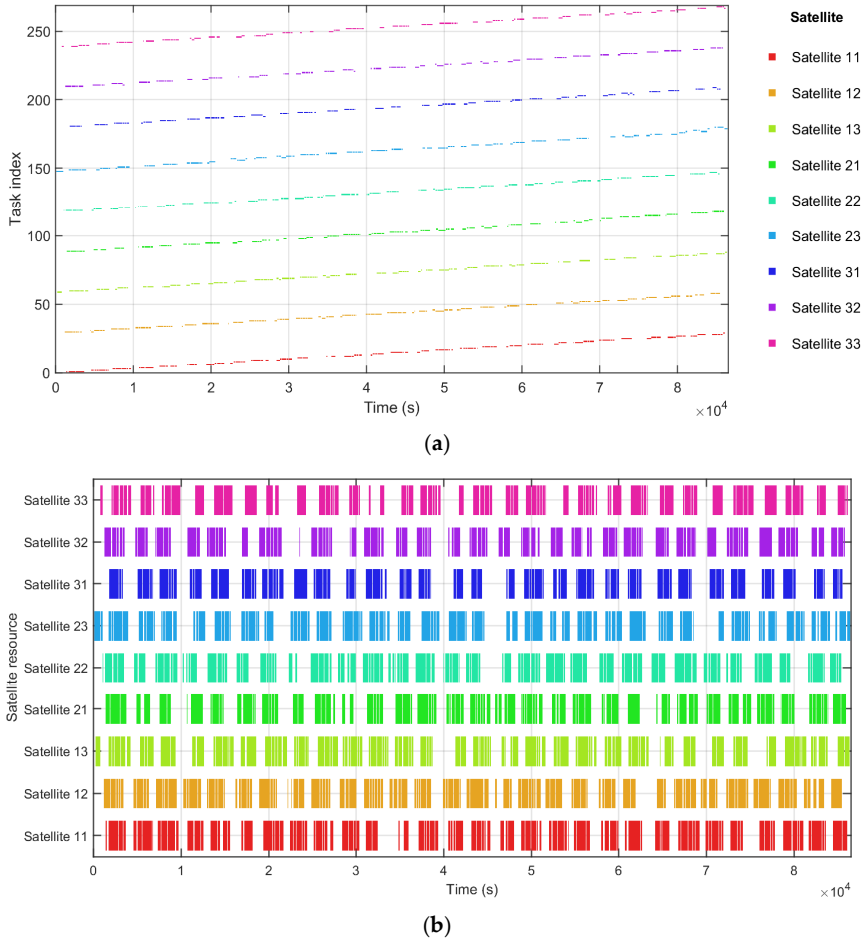

Figure 8. Representative task-level and satellite-resource scheduling views generated by AMOREA. (**a**) Task-level scheduling distribution across the planning horizon; (**b**) satellite-resource occupation distribution across nine remote sensing satellites.

Figure 8b presents the scheduling result from the satellite-resource perspective. Each horizontal lane corresponds to one remote sensing satellite resource, including Satellites 11–13, Satellites 21–23, and Satellites 31–33. The colored bars indicate the time intervals occupied by scheduled transmission slices. The dense but separated occupation patterns show

that AMOREA can coordinate multiple satellite resources while satisfying satellite-side exclusivity, link-establishment overhead, and switching protection constraints.

Figure 9 shows the completion ratios and slicing details of ten randomly selected tasks from the global task pool under different algorithms. These tasks cover different priority levels and provide an intuitive task-level comparison of the scheduling behaviours of the algorithms.

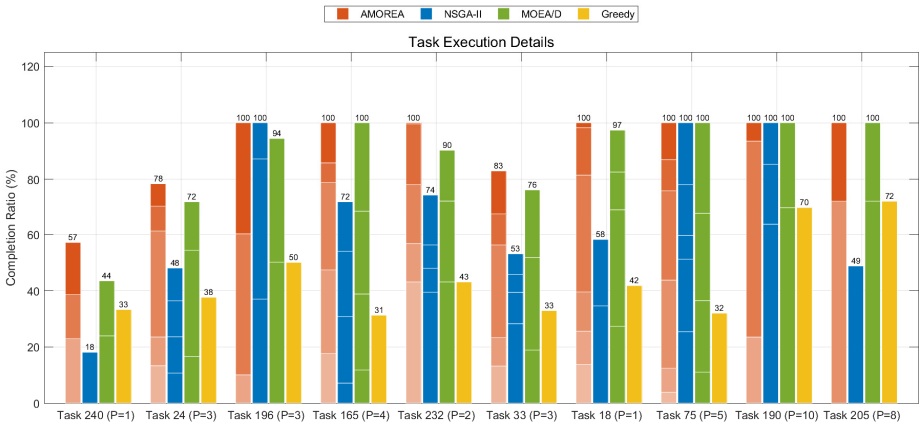

Figure 9. Completion ratios and slicing details of randomly selected tasks under different algorithms.

AMOREA achieves relatively high and stable completion ratios across the sampled tasks. Among the ten tasks, AMOREA completes seven tasks at 100%, including high-priority tasks with priorities 8 and 10. For the remaining tasks, it still maintains relatively high completion ratios, indicating that the adaptive reconstruction mechanism can effectively allocate fragmented visible-window resources under strict link-establishment and resource-exclusivity constraints.

MOEA/D also obtains competitive results for several tasks and reaches full completion in some cases, but its performance is less stable across the sampled tasks. NSGA-II shows larger fluctuations: it achieves full completion for some tasks but performs much worse for others. Greedy generally obtains lower completion ratios because it lacks a global multi-objective search mechanism and tends to make locally optimal window-selection decisions.

The tasks shown in Figure 9 are randomly selected examples rather than specially chosen best-case results. Therefore, this figure provides an intuitive illustration of task-level scheduling behaviour, while the overall multi-objective performance is primarily evaluated using the statistical HV results in Table 6.

Figure 10 compares the task completion rates of AMOREA, NSGA-II, MOEA/D, and Greedy under the tested nine remote sensing satellites and 600 LEO communication nodes scenario. AMOREA achieves a 100.0% completion rate for urgent high-priority tasks, indicating that the proposed priority-aware scheduling mechanism can effectively protect mission-critical transmissions under strong resource competition. MOEA/D also achieves a relatively high urgent-task completion rate of 98.3%, whereas NSGA-II and Greedy reach 90.9% and 62.1%, respectively.

For low-priority daily tasks, AMOREA maintains the highest completion rate of 87.2%, outperforming MOEA/D, NSGA-II, and Greedy by 9.9, 19.0, and 47.5 percentage points, respectively. This result indicates that AMOREA does not simply prioritize urgent tasks at the expense of routine tasks; instead, through adaptive decomposition–reconstruction and multi-objective optimization, it can more effectively reuse fragmented visible windows across different task priorities.

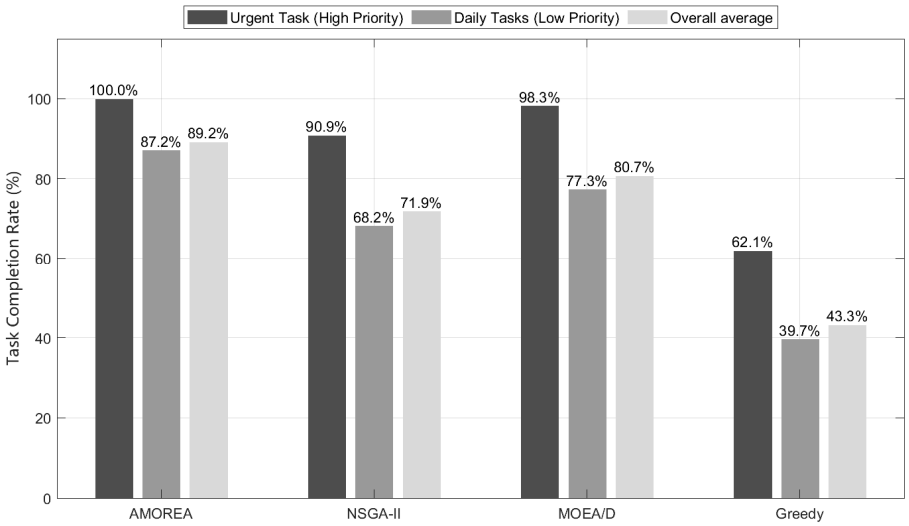

Figure 10. Comparison of task completion rates by priority level.

In terms of the overall average completion rate, AMOREA achieves 89.2%, which is higher than MOEA/D, NSGA-II, and Greedy, whose completion rates are 80.7%, 71.9%, and 43.3%, respectively. These results demonstrate that AMOREA provides stronger task-service capability in the 9 remote sensing satellites and 600 LEO communication nodes scenario by jointly balancing priority-weighted transmission benefit, slicing cost, and node-load distribution.

5. Discussion

The simulation results demonstrate the effectiveness of AMOREA in the tested dense-access scenario involving nine remote sensing satellites and 600 LEO communication nodes. The visible-window length distribution, conflict-window ratio, and communication-node hotspot statistics indicate that the constructed scenario exhibits evident visible-window fragmentation, node-level resource competition, and local access hotspots. Therefore, this scenario provides a representative environment for evaluating multi-satellite scheduling under strong resource conflicts, strict resource-exclusivity constraints, and non-negligible laser link-establishment overhead.

However, compared with future large-scale integrated LEO networks that may consist of hundreds of remote sensing satellites and thousands of LEO communication satellites, the current simulation scale remains limited. The experimental results in this paper mainly verify the effectiveness of AMOREA under a representative dense-access scenario, rather than fully covering all the complexity that may arise in future ultra-large-scale LEO integrated networks. Future work will construct larger-scale simulation scenarios to further evaluate the scalability, convergence behavior, computational cost, and practical applicability of the proposed method under higher task concurrency, denser visible-window distributions, and more severe node-level competition. In addition, parallel implementation and acceleration strategies may be explored to improve the applicability of AMOREA to large-scale constellation scheduling problems.

In the current performance evaluation, the hypervolume (HV) metric is adopted as the primary indicator because it jointly reflects the convergence and diversity of the obtained Pareto solution sets. Although the current HV-based results are sufficient to demonstrate the comparative advantages of AMOREA under the tested scenario, additional multi-objective performance indicators, such as the inverted generational distance (IGD), can be introduced in future studies to provide a more comprehensive evaluation of Pareto-front approximation quality.

In addition, although AMOREA improves scheduling performance in the tested scenario, service delay, average waiting time, and dynamic priority adjustment for postponed routine tasks are not explicitly optimized in the current model. Future work will consider rolling-horizon scheduling with waiting-time-aware or deadline-aware priority adjustment to reduce starvation risk and improve long-term service fairness in continuous operation scenarios.

6. Conclusions

This paper proposes an Adaptive Multi-Objective Reconstruction Evolutionary Algorithm (AMOREA) for scheduling data transmission from dense remote sensing satellites through LEO mobile communication constellations. To address highly dynamic LEO-LEO relative motion, fragmented visible windows, laser link-establishment overhead, and strict satellite and node resource exclusivity, a three-objective scheduling model is established. The model jointly considers priority-weighted transmission utility, slicing and link-establishment cost, and communication-node load imbalance.

AMOREA combines hybrid initialization, task-level adaptive decomposition, multi-strategy reconstruction, and adaptive operator-weight feedback. These mechanisms allow the algorithm to release and reorganize spatiotemporal resources at the task level, thereby improving its ability to aggregate fragmented visible windows and resolve local resource conflicts under dense multi-satellite access conditions.

Simulation results based on the STK-MATLAB scenario show that AMOREA achieves the best overall Pareto performance among the compared algorithms. Its mean HV reaches 8484.6 ± 152.94, which is approximately 19.1% higher than NSGA-II, 17.6% higher than MOEA/D, and 67.6% higher than the Greedy baseline. Under the specific simulation configuration with nine remote sensing satellites and 600 LEO communication nodes, AMOREA achieves a 100.0% completion rate for urgent high-priority tasks and an overall average task completion rate of 89.2%. These results indicate that the proposed adaptive reconstruction mechanism can effectively improve Pareto solution quality and task-service capability in highly dynamic and resource-constrained LEO-LEO scheduling scenarios.

Author Contributions: Conceptualization, D.Z. and J.W.; methodology, A.S.; validation, A.S. and J.W.; formal analysis, G.Y. and X.S.; investigation, A.S. and Y.T.; data curation, A.S. and J.W.; writing—original draft preparation, A.S.; writing—review and editing, Y.T. and G.Y.; visualization, A.S.; supervision, D.Z. and X.S. All authors have read and agreed to the published version of the manuscript.

Funding: This research received no external funding.

Data Availability Statement: The data presented in this study are available on request from the corresponding author.

Acknowledgments: The authors are grateful for the support and help of lab teachers and classmates.

Conflicts of Interest: Author Jiao Wang was employed by China Satellite Network Innovation Co., Ltd. The remaining authors declare that the research was conducted in the absence of any commercial or financial relationships that could be construed as a potential conflict of interest.

Abbreviations

The following abbreviations are used in this manuscript:

AMOREA	Adaptive Multi-Objective Reconstruction Evolutionary Algorithm
LEO	low-Earth orbit
GEO	geostationary orbit
PAT	pointing, acquisition, and tracking

References

1. Jiang, B. The development and prospect of China's space earth observation technology. *Acta Geod. Cartogr. Sin.* **2022**, *51*, 1153–1159. Available online: https://link.cnki.net/urlid/11.2089.P.20220425.1139.002 (accessed on 28 May 2026).
2. Ferrari, B.; Cordeau, J.-F.; Delorme, M.; Iori, M.; Orosei, R. Satellite Scheduling Problems: A Survey of Applications in Earth and Outer Space Observation. *Comput. Oper. Res.* **2025**, *173*, 106875. [CrossRef]
3. Dixon, C.; Olshefski, D.; Jain, V.; DeCusatis, C.; Felter, W.; Carter, J.; Banikazemi, M.; Mann, V.; Tracey, J.M.; Recio, R. Software Defined Networking to Support the Software Defined Environment. *IBM J. Res. Dev.* **2014**, *58*, 3:1–3:14. [CrossRef]
4. Tian, L.; Tian, J.; Jiang, B. Challenges and research on remote sensing satellite application technology in the Giant Constellation Era. *Natl. Remote Sens. Bull.* **2024**, *28*, 1658–1666. [CrossRef]
5. Kassas, Z.M.; Kozhaya, S.; Kanj, H.; Saroufim, J.; Hayek, S.W.; Neinavaie, M.; Khairallah, N.; Khalife, J. Navigation with Multi-Constellation LEO Satellite Signals of Opportunity: Starlink, OneWeb, Orbcomm, and Iridium. In *Proceedings of the 2023 IEEE/ION Position, Location and Navigation Symposium (PLANS)*; IEEE: New York, NY, USA, 2023; pp. 338–343. [CrossRef]
6. Vazquez, A.J.; Erwin, R.S. On the Tractability of Satellite Range Scheduling. *Optim. Lett.* **2015**, *9*, 311–327. [CrossRef]
7. Jia, L.; Zhang, Y.; Yu, J.; Wang, X. Design of Mega-Constellations for Global Uniform Coverage with Inter-Satellite Links. *Aerospace* **2022**, *9*, 234. [CrossRef]
8. Bhattacharjee, D.; Madoery, P.G.; Chaudhry, A.U.; Yanikomeroglu, H.; Kurt, G.K.; Hu, P.; Ahmed, K.; Martel, S. On-Demand Routing in LEO Mega-Constellations with Dynamic Laser Inter-Satellite Links. *IEEE Trans. Aerosp. Electron. Syst.* **2024**, *60*, 7089–7105. [CrossRef]
9. Kim, S.J.; Kim, M.; Kim, C.-H.; Choi, H.-L. Satellite Scheduling Framework of Observation-Relay-Downlink with a Mixed-Integer Linear Programming Model. In *AIAA SCITECH 2025 Forum*; American Institute of Aeronautics and Astronautics: Orlando, FL, USA, 2025; pp. 2025–2273. [CrossRef]
10. Sun, G.; Peng, S.; Chen, H.; Wu, J.; Li, J. Multi-objective optimization method oriented to integrated scenario of TT&C resources and data transmission resources. *Acta Aeronaut. Astronaut. Sin.* **2022**, *43*, 661–677. [CrossRef]
11. Chen, X.; Reinelt, G.; Dai, G.; Spitz, A. A Mixed Integer Linear Programming Model for Multi-Satellite Scheduling. *Eur. J. Oper. Res.* **2019**, *275*, 694–707. [CrossRef]
12. Lee, M.; Yu, S.; Kwon, K.; Lee, M.; Lee, J.; Kim, H. Mixed-Integer Linear Programming Model for Scheduling Missions and Communications of Multiple Satellites. *Aerospace* **2024**, *11*, 83. [CrossRef]
13. Xiao, Y.; Zhang, S.; Yang, P.; You, M.; Huang, J. A Two-Stage Flow-Shop Scheme for the Multi-Satellite Observation and Data-Downlink Scheduling Problem Considering Weather Uncertainties. *Reliab. Eng. Syst. Saf.* **2019**, *188*, 263–275. [CrossRef]
14. Xhafa, F.; Herrero, X.; Barolli, A.; Barolli, L.; Takizawa, M. Evaluation of Struggle Strategy in Genetic Algorithms for Ground Stations Scheduling Problem. *J. Comput. Syst. Sci.* **2013**, *79*, 1086–1100. [CrossRef]
15. Long, J.; Wu, S.; Han, X.; Wang, Y.; Liu, L. Autonomous Task Planning Method for Multi-Satellite System Based on a Hybrid Genetic Algorithm. *Aerospace* **2023**, *10*, 70. [CrossRef]
16. Herrmann, A.; Schaub, H. Reinforcement Learning for the Agile Earth-Observing Satellite Scheduling Problem. *IEEE Trans. Aerosp. Electron. Syst.* **2023**, *59*, 5235–5247. [CrossRef]
17. Xiang, S.; Liang, Q.; Tang, P. Task-Oriented Compression Framework for Remote Sensing Satellite Data Transmission. *IEEE Trans. Ind. Inform.* **2024**, *20*, 3487–3496. [CrossRef]
18. Zhang, J.; Xing, L. An Improved Genetic Algorithm for the Integrated Satellite Imaging and Data Transmission Scheduling Problem. *Comput. Oper. Res.* **2022**, *139*, 105626. [CrossRef]
19. Chen, H.; Zhai, B.; Wu, J.; Du, C.; Li, J. A Satellite Observation Data Transmission Scheduling Algorithm Oriented to Data Topics. *Int. J. Aerosp. Eng.* **2020**, *2020*, 2180674. [CrossRef]
20. Chen, H.; Sun, G.; Peng, S.; Wu, J. Dynamic rescheduling method for TT&C and data transmission resources based on multi-objective optimization. *Syst. Eng. Electron.* **2024**, *46*, 3744–3753. Available online: https://link.cnki.net/urlid/11.2422.TN.20230220.1046.006 (accessed on 28 May 2026).
21. Zhou, C.; Zhang, C.; Li, C. Fragment consolidation based scheduling algorithm for TT&C and data transmission. *Syst. Eng. Electron.* **2026**, *48*, 1946–1964. Available online: https://link.cnki.net/urlid/11.2422.tn.20260320.1515.041 (accessed on 28 May 2026).
22. Chang, Z.; Punnen, A.P.; Zhou, Z.; Cheng, S. Solving Dynamic Satellite Image Data Downlink Scheduling Problem via an Adaptive Bi-Objective Optimization Algorithm. *Comput. Oper. Res.* **2023**, *160*, 106388. [CrossRef]
23. Zhang, J.; Xing, L.; Peng, G.; Yao, F.; Chen, C. A Large-Scale Multiobjective Satellite Data Transmission Scheduling Algorithm Based on SVM+NSGA-II. *Swarm Evol. Comput.* **2019**, *50*, 100560. [CrossRef]
24. Qu, Q.; Liu, K.; Li, X.; Zhou, Y.; Lü, J. Satellite Observation and Data-Transmission Scheduling Using Imitation Learning Based on Mixed Integer Linear Programming. *IEEE Trans. Aerosp. Electron. Syst.* **2023**, *59*, 1989–2001. [CrossRef]
25. Chen, X.; Gu, W.; Dai, G.; Xing, L.; Tian, T.; Luo, W.; Cheng, S.; Zhou, M. Data-Driven Collaborative Scheduling Method for Multi-Satellite Data-Transmission. *Tsinghua Sci. Technol.* **2024**, *29*, 1463–1480. [CrossRef]

26. Ou, J.; Xing, L.; Yao, F.; Li, M.; Lv, J.; He, Y.; Song, Y.; Wu, J.; Zhang, G. Deep Reinforcement Learning Method for Satellite Range Scheduling Problem. *Swarm Evol. Comput.* **2023**, *77*, 101233. [CrossRef]
27. Li, S.; Yu, Q.; Ding, H. Reviews and Prospects in Satellite Range Scheduling Problem. *Auton. Intell. Syst.* **2023**, *3*, 9–24. [CrossRef]
28. Wang, X.; Wu, G.; Xing, L.; Pedrycz, W. Agile Earth Observation Satellite Scheduling over 20 Years: Formulations, Methods, and Future Directions. *IEEE Syst. J.* **2021**, *15*, 3881–3892. [CrossRef]
29. Hassan, N.U.L.; Huang, C.; Yuen, C.; Ahmad, A.; Zhang, Y. Dense Small Satellite Networks for Modern Terrestrial Communication Systems: Benefits, Infrastructure, and Technologies. *IEEE Wirel. Commun.* **2020**, *27*, 96–103. [CrossRef]
30. del Portillo, I.; Cameron, B.G.; Crawley, E.F. A Technical Comparison of Three Low Earth Orbit Satellite Constellation Systems to Provide Global Broadband. *Acta Astronaut.* **2019**, *159*, 123–135. [CrossRef]
31. Pan, G.; Ye, J.; An, J.; Alouini, M.-S. Latency versus Reliability in LEO Mega-Constellations: Terrestrial, Aerial, or Space Relay? *IEEE Trans. Mob. Comput.* **2023**, *22*, 5330–5345. [CrossRef]
32. Li, R.; Lin, B.; Liu, Y.; Shen, Y.; Dong, M.; Zhao, S.; Kong, C.; Liu, E.; Lin, X. Review on laser intersatellite link: Current status, trends, and prospects. *Infrared Laser Eng.* **2023**, *52*, 133–147. [CrossRef]
33. Verma, S.; Pant, M.; Snasel, V. A Comprehensive Review on NSGA-II for Multi-Objective Combinatorial Optimization Problems. *IEEE Access* **2021**, *9*, 57757–57791. [CrossRef]
34. Bhattacharjee, D.; Chaudhry, A.U.; Yanikomeroglu, H.; Hu, P.; Lamontagne, G. Laser Inter-Satellite Link Setup Delay: Quantification, Impact, and Tolerable Value. In *Proceedings of the 2023 IEEE Wireless Communications and Networking Conference (WCNC)*; IEEE: New York, NY, USA, 2023; pp. 1–6. [CrossRef]